Journal of Computational Physics 394 (2019) 719–731

Contents lists available at ScienceDirect

Journal of Computational Physics

www.elsevier.com/locate/jcp

Local discontinuous Galerkin methods with implicit-explicit multistep time-marching for solving the nonlinear Cahn-Hilliard equation

Hui Shi [a], Ying Li [a,b,*]

[a] School of Computer Engineering and Science, Shanghai University, Shanghai, 200444, PR China
[b] Shanghai Institute for Advanced Communication and Data Science, Shanghai University, Shanghai, 200444, PR China

ARTICLE INFO

Article history:
Received 4 January 2019
Received in revised form 20 May 2019
Accepted 26 May 2019
Available online 10 June 2019

Keywords:
Cahn-Hilliard equation
Local discontinuous Galerkin
Implicit-explicit multistep scheme
Nonlinear

ABSTRACT

In this paper, we develop the fully discrete local discontinuous Galerkin (LDG) methods coupled with the implicit-explicit (IMEX) multistep time marching for solving the nonlinear Cahn-Hilliard equation. To be more specific, we rewrite the Cahn-Hilliard equation in a novel form by adding and subtracting a "linear" term. Then we discretize the spatial derivatives with the LDG methods and the temporal derivative with the IMEX multistep method. Finally, a series of numerical experiments are given to verify the accuracy, efficiency and validness of proposed method.

1. Introduction

In this paper, we consider the Cahn-Hilliard (CH) equation in a bounded domain $\Omega \in \mathbb{R}^d$ $(d \leq 3)$ [1]

$$u_t = \nabla \cdot \left(b(u) \nabla \left(-\gamma \Delta u + \Psi'(u) \right) \right), (x,t) \in \Omega \times (0,T], \tag{1}$$

Here, $b(u)$ is the non-negative diffusion mobility, $\Psi(u)$ is the homogeneous free energy density, and γ is a positive constant. The equation simulates the process that a two-phase alloy fluid separates into domains of pure of each component. The phase function $u \in [-1,1]$ represents the concentration of each component, and the reaction term $\Psi'(u)$ drives the solution to the two pure states $u = \pm 1$.

The total free energy $E(u)$ can be defined by

$$E(u) = \int_\Omega \left(\frac{\gamma}{2} |\nabla u|^2 + \Psi(u) \right) dK. \tag{2}$$

By differentiating the above energy $E(u)$, we can get

$$\frac{d}{dt} E(u) = \int_\Omega \left(\gamma |\nabla u| \cdot |\nabla u_t| + \Psi'(u) u_t \right) dK \tag{3}$$

* Corresponding author.
E-mail addresses: shihui17@shu.edu.cn (H. Shi), yinglotus@shu.edu.cn (Y. Li).

https://doi.org/10.1016/j.jcp.2019.05.040
0021-9991/

$$= \int_{\Omega} \left(\Psi'(u) - \gamma \Delta u\right) \cdot u_t dK \tag{4}$$

$$= -\int_{\Omega} \left(\nabla \left(\Psi'(u) - \gamma \Delta u\right)\right)^2 dK \leq 0. \tag{5}$$

Therefore, the total energy $E(u)$ is non-increasing in time for the solution $u(x,t)$ of the Cahn-Hilliard equation.

The Cahn-Hilliard equation was originally introduced by Cahn and Hilliard [2] to describe the phenomenon of phase separation and phase coarsening in binary alloys, which has been widely used in many complicated moving interface problems in materials science and fluid dynamics [1,3–13]. However, the fourth order spatial derivative term and the nonlinear term of the Cahn-Hilliard equation make two difficulties for the numerical simulation: (1) the strong discontinuities in solutions, and (2) the stringent time step restriction of explicit schemes. Therefore, constructing stable and efficient numerical schemes is important.

The first difficulty is overcome by the local discontinuous Galerkin (LDG) methods in this paper. We know that the LDG methods have been successfully designed for solving the partial differential equations (PDEs) containing higher order spatial derivatives, such for the Zakharov system [14], the Cahn-Hilliard equations [1,10], the KdV type equations [15,16], the carburizing model [38], etc. The first LDG method was constructed by Cockburn and Shu in [17] for solving the nonlinear convection diffusion equations containing second order spatial derivatives, motivated by the successful numerical experiments of Bassi and Rebay [18] for the compressible Navier-Stokes equations. The main idea of the LDG method is to rewrite the equations with higher order derivatives as an equivalent first order system, then apply the discontinuous Galerkin (DG) method to the system with suitable numerical fluxes. We refer readers to the original papers [19–24] for more details about the DG method.

The implicit-explicit (IMEX) multistep method is applied to solve the second difficulty. The IMEX methods can cope with both the shortcomings of the fully explicit and implicit time discretization methods. Explicit time-marching always suffers from small time step restriction for stability, and implicit time-marching may be structurally difficult or computationally costly. Accordingly, several attempts have been made to apply the IMEX methods to deal with the time-dependent PDEs, for example IMEX Runge-Kutta methods, IMEX multistep methods and their deformations [25–37]. Recently, Wang et al. in [26] proposed two specific IMEX Runge-Kutta LDG schemes for solving one-dimensional nonlinear diffusion problems $U_t = (a(U)U_x)_x$. The highlight is to add and subtract a constant diffusion term $a_0 U_{xx}$ on the right hand side of the original equation, then to treat the linear term $a_0 U_{xx}$ implicitly and the nonlinear term $(a(U)U_x)_x - a_0 U_{xx}$ explicitly. The results showed that their first and second schemes were stable and efficient when they selected appropriate a_0. Meanwhile, they gave the guidance for the choice of a_0. Therefore, we extend the new technique to the Cahn-Hilliard equation in this paper. Numerical experiments are carried out to verify the accuracy, efficiency and validness of the proposed method.

The paper is organized as follows. In Section 2, we present the IMEX multistep LDG methods for the nonlinear Cahn-Hilliard equation. Section 3 contains several numerical experiments both in one and two dimensions. Results demonstrate the accuracy and capability of the new methods. Finally, conclusions are given in Section 4.

2. The IMEX multistep LDG method for the Cahn-Hilliard equation

2.1. Notation

Let $\mathcal{T}_h$ denote a tessellation of Ω with shape-regular elements K. Let Γ denote the union of the boundary faces of elements $K \in \mathcal{T}_h$, i.e. $\Gamma = \cup_{K\in\mathcal{T}_h} \partial K$, and $\Gamma_0 = \Gamma \backslash \partial\Omega$. Let $\mathcal{P}^k(K)$ be the space of polynomials of degree at most $k \geq 0$ on $K \in \mathcal{T}_h$. The finite element spaces are denoted by

$$V_h = \left\{ v \in L^2(\Omega) : v|_K \in \mathcal{P}^k(K), \forall K \in \mathcal{T}_h \right\}, \tag{6}$$

$$\Sigma_h = \left\{ \phi = (\phi_1, \cdots, \phi_N)^T : \phi_i|_K \in \mathcal{P}^k(K), i = 1, \cdots, N, \forall K \in \mathcal{T}_h \right\}. \tag{7}$$

Note that functions in V_h and Σ_h are allowed to be completely discontinuous across element interfaces, which are allowed to have jumps at the interfaces ∂K. At each element interface point, for any piecewise function p, there are two traces along the right-hand and left-hand, denoted by p^+ and p^-, respectively. The jump is denoted by $[\![p]\!] = p^+ - p^-$.

2.2. The semi-discrete LDG scheme

To begin with our numerical method, we rewrite the Eq. (1) as the following equivalent second order system:

$$u_t = \nabla \cdot (b(u) \nabla \beta), \tag{8a}$$

$$\beta = -\gamma \Delta u + \Psi'(u). \tag{8b}$$

Here, β denotes the chemical potential. Then we construct a new form by adding and subtracting a "linear" term $a_0\Delta\beta$ on the right hand side of the Eqs. (8). Notice that the new term $a_0\Delta\beta$ contains a nonlinear function $\Psi'(u)$.

$$u_t = \nabla\cdot\left(b(u)\nabla\beta - a_0\nabla\beta\right) + a_0\Delta\beta, \tag{9a}$$

$$\beta = -\gamma\Delta u + \Psi'(u). \tag{9b}$$

To define the LDG method, we rewrite the Eqs. (9) as the following equivalent first order system:

$$u_t = \nabla\cdot\left(b(u)\boldsymbol{q} - a_0\boldsymbol{q}\right) + a_0\nabla\cdot\boldsymbol{q}, \tag{10a}$$

$$\boldsymbol{q} = \nabla\beta, \tag{10b}$$

$$\beta = -\gamma\nabla\cdot\boldsymbol{w} + r, \tag{10c}$$

$$\boldsymbol{w} = \nabla u, \tag{10d}$$

$$r = \Psi'(u). \tag{10e}$$

The semi-discrete LDG scheme is to find $u,\beta,r\in V_h$ and $\boldsymbol{q},\boldsymbol{w}\in\Sigma_h$, such that, for all test functions $\rho,\xi,\psi\in V_h$ and $\eta,\phi\in\Sigma_h$, we have

$$(u_t,\rho) = \left[\tilde{\mathcal{L}}(b(u)\boldsymbol{q},\rho) - a_0\mathcal{L}(\boldsymbol{q},\rho)\right] + a_0\mathcal{L}(\boldsymbol{q},\rho), \tag{11a}$$

$$(\boldsymbol{q},\eta) = \mathcal{K}(\beta,\eta), \tag{11b}$$

$$(\beta,\xi) = -\gamma\mathcal{M}(\boldsymbol{w},\xi) + (r,\xi), \tag{11c}$$

$$(\boldsymbol{w},\phi) = \mathcal{N}(u,\phi), \tag{11d}$$

$$(r,\psi) = \left(\Psi'(u),\psi\right), \tag{11e}$$

where

$$\tilde{\mathcal{L}}(b(u)\boldsymbol{q},\rho) = -\sum_{j=1}^{N}\left[(b(u)\boldsymbol{q},\rho_x)_j - \left(\widehat{b(u)\hat{\boldsymbol{q}}}\right)_{j+\frac12}\rho^-_{j+\frac12} + \left(\widehat{b(u)\hat{\boldsymbol{q}}}\right)_{j-\frac12}\rho^+_{j-\frac12}\right], \tag{12a}$$

$$\mathcal{L}(\boldsymbol{q},\rho) = -\sum_{j=1}^{N}\left[(\boldsymbol{q},\rho_x)_j - \hat{\boldsymbol{q}}_{j+\frac12}\rho^-_{j+\frac12} + \hat{\boldsymbol{q}}_{j-\frac12}\rho^+_{j-\frac12}\right], \tag{12b}$$

$$\mathcal{K}(\beta,\eta) = -\sum_{j=1}^{N}\left[(\beta,\eta_x)_j - \hat{\beta}_{j+\frac12}\eta^-_{j+\frac12} + \hat{\beta}_{j-\frac12}\eta^+_{j-\frac12}\right], \tag{12c}$$

$$\mathcal{M}(\boldsymbol{w},\xi) = -\sum_{j=1}^{N}\left[(\boldsymbol{w},\xi_x)_j - \hat{\boldsymbol{w}}_{j+\frac12}\xi^-_{j+\frac12} + \hat{\boldsymbol{w}}_{j-\frac12}\xi^+_{j-\frac12}\right], \tag{12d}$$

$$\mathcal{N}(u,\phi) = -\sum_{j=1}^{N}\left[(u,\phi_x)_j - \hat{u}_{j+\frac12}\phi^-_{j+\frac12} + \hat{u}_{j-\frac12}\phi^+_{j-\frac12}\right]. \tag{12e}$$

The "hat" terms in Eqs. (12) are the so-called "numerical fluxes", which are functions defined on the edges and should be designed to ensure stability.

We can take the simple choices such that

$$\hat{\boldsymbol{w}} = \boldsymbol{w}^-, \quad \hat{\beta} = \beta^+, \quad \hat{\boldsymbol{q}} = \boldsymbol{q}^-, \quad \hat{u} = u^+. \tag{13}$$

We remark that the choice for the fluxes Eq. (13) is not unique. In fact the crucial part is taking $\hat{\boldsymbol{q}},\hat{\boldsymbol{w}}$ and $\hat{\beta},\hat{u}$ from opposite sides.

2.3. The full discretization

In this subsection, we would like to consider the IMEX multistep method for temporal discretization.

Let $\left\{t^n = n\tau\right\}_{n=0}^{M}$ be the uniform partition of the time interval $[0,T]$, with time step τ. In this paper, we take the time step as a constant for simplicity. Given u^n, we would like to find the numerical solution at the next time level t^{n+1}.

We can define the approximation u_h^n to the nodal values $u(x,t^n)$ of the exact solution as follows:

$$\frac{1}{\tau}\left(\sum_{j=0}^{k}\varsigma_j u_h^{n+j},\rho\right)=\sum_{j=0}^{k-1}\kappa_j\left[\tilde{\mathcal{L}}\left(b\left(u_h^{n+j}\right)\boldsymbol{q}^{n+j},\rho\right)-a_0\mathcal{L}\left(\boldsymbol{q}^{n+j},\rho\right)\right]+a_0\mathcal{L}\left(\boldsymbol{q}^{n+k},\rho\right), \tag{14}$$

where ς_j and κ_j are the coefficients of z^j of the following polynomials a and c, respectively.

$$a(z)=\sum_{j=1}^{k}\frac{1}{j}z^{k-j}(z-1)^j,\ b(z)=z^k,\ c(z)=z^k-(z-1)^k, \tag{15}$$

where the polynomials (a,b) are used to get the coefficients of the implicit k-step backward differentiation formula (BDF) method and the polynomials (a,c) are used to get the coefficients of the explicit k-step method.

Accordingly, we can derive the following one-step and two-step fully discretization formulations of Eqs. (11) by taking $k=1,2$ in Eq. (14), respectively.

The one-step IMEX multistep LDG method can be written as

$$\left(\frac{u^{n+1}-u^n}{\tau},\rho\right)=\left[\tilde{\mathcal{L}}\left(b\left(u^n\right)\boldsymbol{q}^n,\rho\right)-a_0\mathcal{L}\left(\boldsymbol{q}^n,\rho\right)\right]+a_0\mathcal{L}\left(\boldsymbol{q}^{n+1},\rho\right), \tag{16a}$$

$$\left(\boldsymbol{q}^{n,l},\eta\right)=\mathcal{K}\left(\beta^{n,l},\eta\right),\quad \text{for}\quad l=0,1, \tag{16b}$$

$$\left(\beta^{n,l},\xi\right)=-\gamma\mathcal{M}\left(\boldsymbol{w}^{n,l},\xi\right)+\left(r^{n,l-1},\xi\right),\quad \text{for}\quad l=0,1, \tag{16c}$$

$$\left(\boldsymbol{w}^{n,l},\phi\right)=\mathcal{N}\left(u^{n,l},\phi\right),\quad \text{for}\quad l=0,1, \tag{16d}$$

$$\left(r^{n,l},\psi\right)=\left(\Psi'\left(u^{n,l}\right),\psi\right),\quad \text{for}\quad l=0, \tag{16e}$$

where $s^{n,-1}=s^n$, $s^{n,0}=s^n$ and $s^{n,1}=s^{n+1}$.

The two-step IMEX multistep LDG method is given as follows:

$$\left(\frac{3u^{n+1}-4u^n+u^{n-1}}{2\tau},\rho\right)=2\left[\tilde{\mathcal{L}}\left(b\left(u^n\right)\boldsymbol{q}^n,\rho\right)-a_0\mathcal{L}\left(\boldsymbol{q}^n,\rho\right)\right]-\left[\tilde{\mathcal{L}}\left(b\left(u^{n-1}\right)\boldsymbol{q}^{n-1},\rho\right)-a_0\mathcal{L}\left(\boldsymbol{q}^{n-1},\rho\right)\right]$$
$$+a_0\mathcal{L}\left(\boldsymbol{q}^{n+1},\rho\right), \tag{17a}$$

$$\left(\boldsymbol{q}^{n,l},\eta\right)=\mathcal{K}\left(\beta^{n,l},\eta\right),\quad \text{for}\quad l=0,1,2, \tag{17b}$$

$$\left(\beta^{n,l},\xi\right)=-\gamma\mathcal{M}\left(\boldsymbol{w}^{n,l},\xi\right)+\left(r^{n,l-1},\xi\right),\quad \text{for}\quad l=0,1,2, \tag{17c}$$

$$\left(\boldsymbol{w}^{n,l},\phi\right)=\mathcal{N}\left(u^{n,l},\phi\right),\quad \text{for}\quad l=0,1,2, \tag{17d}$$

$$\left(r^{n,l},\psi\right)=\left(\Psi'\left(u^{n,l}\right),\psi\right),\quad \text{for}\quad l=0,1, \tag{17e}$$

where $s^{n,-1}=s^{n-1}$, $s^{n,0}=s^{n-1}$, $s^{n,1}=s^n$ and $s^{n,2}=s^{n+1}$.

Notice that the terms containing the nonlinear function $\Psi'(u)$ are treated explicitly.

3. Numerical results

In this section, we validate the accuracy and performance of the IMEX multistep LDG schemes numerically. In section 3.1, three one-dimensional examples are given to test the accuracy of the algorithm proposed, and in section 3.2, four two-dimensional shape relaxation examples are shown to illustrate the performance of the method.

3.1. Rates of convergence study

In the following three experiments, we take different diffusion mobility $b(u)$. In Example 1 and Example 2, $b(u)=1$, and $b(u)=1-\sin(x)$ in Example 3. Moreover, we take $a_0=0.4,0.5,1,10$ in Example 1, 2 and $a_0=0.5,1,2,10$ in Example 3 to test the effect of different a_0.

Table 1
The L^∞ errors and orders of accuracy for Example 1: $b(u) = 1$.

	N	$a_0 = 0.4$		$a_0 = 0.5$		$a_0 = 1$		$a_0 = 10$	
		L^∞ error	Order	L^∞ error	Order	L^∞ error	Order	L^∞ error	Order
P^0 with Eqs. (16)	10	4.42E-01	–	4.52E-01	–	4.63E-01	–	4.67E-01	–
	20	2.04E-01	1.12	2.10E-01	1.11	2.17E-01	1.09	2.23E-01	1.07
	40	9.91E-02	1.04	1.02E-01	1.04	1.09E-02	1.00	1.11E-01	1.01
	80	4.92E-02	1.01	5.03E-02	1.02	5.36E-02	1.02	5.50E-02	1.01
	160	2.46E-02	1.00	2.50E-02	1.01	2.66E-02	1.01	2.73E-02	1.01
	320	1.23E-02	1.00	1.25E-02	1.00	1.32E-02	1.01	1.36E-02	1.01
	640	6.13E-03	1.00	6.22E-03	1.00	6.60E-03	1.00	6.77E-03	1.00
P^1 with Eqs. (17)	10	4.57E-02	–	4.57E-02	–	5.39E-02	–	2.30E-01	–
	20	1.07E-02	2.08	1.07E-02	2.08	1.30E-02	2.05	4.89E-02	2.24
	40	2.61E-03	2.04	2.56E-03	2.06	3.20E-03	2.03	1.31E-02	1.90
	80	6.52E-03	2.00	6.52E-04	1.97	7.97E-04	2.00	3.33E-03	1.97
	160	1.63E-03	2.00	1.63E-04	2.00	1.99E-04	2.00	8.37E-04	1.99
	320	4.05E-05	2.00	4.07E-05	2.00	4.99E-05	2.00	2.10E-04	2.00
	640	1.01E-05	2.00	1.07E-05	1.91	1.18E-05	2.08	5.76E-05	1.87

Example 1. We consider

$$u_t = -\left(b\left(u\right)\left(\gamma u_{xxx} - \left(\Psi'\left(u\right)\right)_x\right)\right)_x, \tag{18}$$

where $\Psi\left(u\right) = \frac{3}{2}\left(1-u^2\right)$, $b(u) = 1$ and $\gamma = 4$ in $\Omega = (0, 4\pi)$ with periodic boundary conditions. The exact solution is

$$u\left(x,t\right) = e^{-t}\sin\left(x\right) - e^{0.5t}\sin\left(0.5x\right). \tag{19}$$

In this example, we take $\tau = 0.001h^3$ for $a_0 = 0.4$, $\tau = 0.1h$ for $a_0 = 0.5, 1$ and $\tau = 0.01h$ for $a_0 = 10$ in P^0 element space. In P^1 element space, we take $\tau = 0.001h^3$ for $a_0 = 0.4$, $\tau = 0.001h$ for $a_0 = 0.5$, $\tau = 0.01h$ for $a_0 = 1$ and $\tau = 0.01h^2$ for $a_0 = 10$. We perform the accuracy tests with respect to τ. And we solve the above mentioned problem for $t = 0.5$. The results are given in Table 1. From Table 1, We can see that the methods with P^k elements give $(k+1)$th order of accuracy in L^∞ norms. The simulation results coincide with the theory.

Fig. 1 shows the numerical solution and the exact solution at $t = 0.5$ using P^1 elements with different a_0 on the uniform mesh with 80 cells. We can observe a good agreement with the exact solution. Meanwhile, there is no obvious difference for different value of a_0 in the numerical experiments.

Example 2. Here, we consider

$$u_t = -\left(b\left(u\right)\left(\gamma u_{xxx} - \left(\Psi'\left(u\right)\right)_x\right)\right)_x, \tag{20}$$

with $b(u) = 1$ and $\gamma = 1$. Taking $\Psi\left(u\right) = \frac{1}{4}\left(1-u^2\right)^2$, we solve the above problem in $\Omega = (0, 2\pi)$ with periodic boundary condition. The exact solution is as follows

$$u\left(x,t\right) = \cos\left(x\right)\cos\left(t\right). \tag{21}$$

Taking $t = 0.5$, the L^∞ errors and the convergence rate for above problem are shown in Table 2. In this example, we take $\tau = 0.001h^3$ for $a_0 = 0.4$ and $\tau = 0.1h$ for $a_0 = 0.5, 1, 10$ in P^0 element space. In P^1 element space, we take $\tau = 0.001h^3$ as the time step. We can see that the methods give $(k+1)$th order of accuracy, which coincide with the theory. And the Fig. 2 shows the numerical solution and the exact solution at $t = 0.5$. Here taking $a_0 = 10$, we use P^1 elements on the uniform mesh with $80, 160, 320, 640$ cells. From the Fig. 2, we can see that the simulation results show good agreement with the exact solution.

Example 3. In this example, we consider the Cahn-Hilliard equation

$$u_t = -\left(b\left(u\right)\left(\gamma u_{xxx} - \left(\Psi'\left(u\right)\right)_x\right)\right)_x, \tag{22}$$

in $\Omega = (0, 2\pi)$ with periodic boundary conditions.

Here, $b(u) = 1 - \sin\left(x\right)$, $\gamma = 2$, and the homogeneous free energy density is

$$\Psi\left(u\right) = \frac{1}{2}\left(1-u^2\right), \tag{23}$$

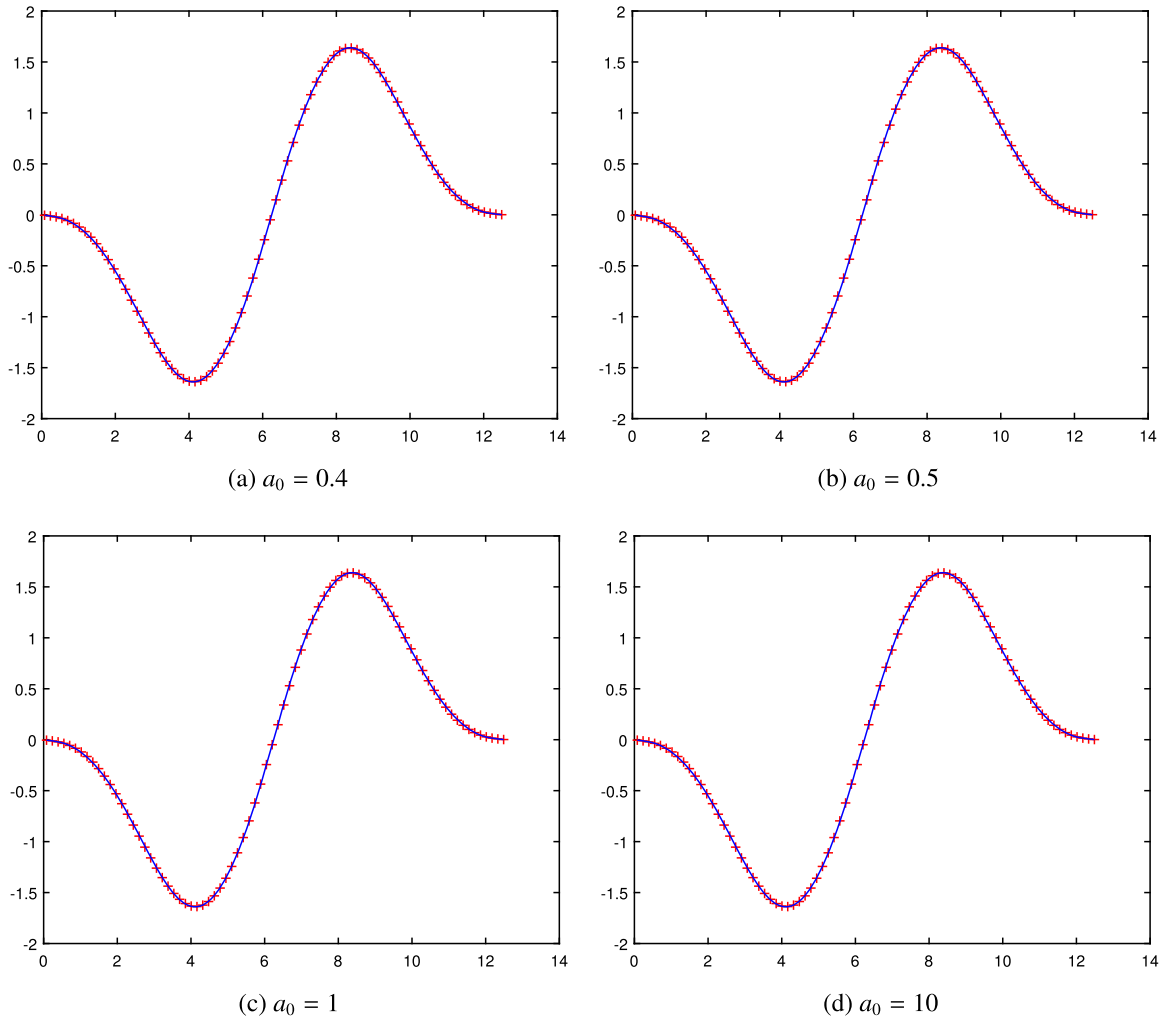

(a) $a_0 = 0.4$ (b) $a_0 = 0.5$

(c) $a_0 = 1$ (d) $a_0 = 10$

Fig. 1. The numerical solution of Eq. Eq. (18) with the initial condition Eq. (19) and periodic boundary condition. $t = 0.5$, $N = 80$.

The exact solution is

$$u(x,t) = e^{-t}\sin(x). \tag{24}$$

Taking $t = 0.5$, the L^∞ errors and the convergence rate for above problem are shown in Table 3. In this example, we relax the diffusion mobility $b(u) = 1 - \sin(x)$, being a direct function of the spatial derivative x. In P^0 element space, we take $\tau = 0.001h^3$ for $a_0 = 0.5$, $\tau = 0.1h$ for $a_0 = 1, 2$ and $\tau = 0.01h$ for $a_0 = 10$. In P^1 element space, we take $\tau = 0.001h^3$ as the time step. From the Table 3, we can notice that numerical results of our schemes satisfy theoretical $(k+1)$-th order of accuracy. And the Fig. 3 shows the numerical solution and the exact solution at $t = 0.5$. Here taking $a_0 = 10$, we use P^1 elements on the uniform mesh with $80, 160, 320, 640$ cells. From the Fig. 3, we can see that the simulation results show good agreement with the exact solution.

Based on the above three experiments, we can notice that the schemes have great performance for both the constant mobility problems and the inconstant mobility problems. Significantly, there is no difference for different value of a_0 in same experiment.

3.2. Numerical Results for the Cahn-Hilliard equation in 2D

In this subsection, we illustrate the performance of the method on four two-dimensional experiments. Example 4 shows the evolution of random initial phase. In Example 5, the initial square deforms into four circles while the original square eventually relax to a circle bubble in Example 6. In Example 7, four bullethead-like bubbles first split into four bubbles, then they deform into four circular bubbles, and finally merge to form two circular bubbles. In all simulations, the problem domain will be partitioned into uniform mesh with 80×80 cells. And the P^0 approximation will be used. Besides, we take $\tau = 0.001h^3$ as the time step.

Table 2
The L^∞ errors and orders of accuracy for Example 2: $b(u) = 1$.

	N	$a_0 = 0.4$		$a_0 = 0.5$		$a_0 = 1$		$a_0 = 10$	
		L^∞ error	Order	L^∞ error	Order	L^∞ error	Order	L^∞ error	Order
P^0 with Eqs. (16)	10	1.37E-01	–	1.37E-01	–	1.37E-01	–	1.37E-01	–
	20	6.84E-02	1.00	6.88E-02	1.00	6.85E-02	1.00	7.10E-02	0.95
	40	3.44E-02	0.99	3.46E-02	0.99	3.45E-02	0.99	3.60E-02	0.98
	80	1.72E-02	0.99	1.73E-02	1.00	1.73E-02	1.00	1.81E-02	0.99
	160	8.65E-03	1.00	8.67E-03	1.00	8.64E-03	1.00	9.08E-03	0.99
	320	4.32E-03	1.00	4.33E-03	1.00	4.32E-03	1.00	4.55E-03	1.00
	640	2.16E-03	1.00	2.17E-03	1.00	2.16E-03	1.00	2.28E-03	1.00
P^1 with Eqs. (17)	10	1.07E-02	–	1.07E-02	–	1.07E-02	–	1.07E-02	–
	20	2.70E-03	1.98	2.70E-03	1.98	2.70E-03	1.98	2.70E-03	1.98
	40	6.76E-04	1.99	6.76E-04	1.99	6.76E-04	1.99	6.76E-04	1.99
	80	1.69E-04	2.00	1.69E-04	2.00	1.69E-04	2.00	1.69E-04	2.00
	160	4.28E-05	1.98	4.28E-05	1.98	4.28E-05	1.98	4.28E-05	1.98
	320	1.05E-05	2.02	1.05E-05	2.02	1.05E-05	2.02	1.05E-05	2.02
	640	2.64E-06	1.99	2.64E-06	1.99	2.64E-06	1.99	2.64E-06	1.99

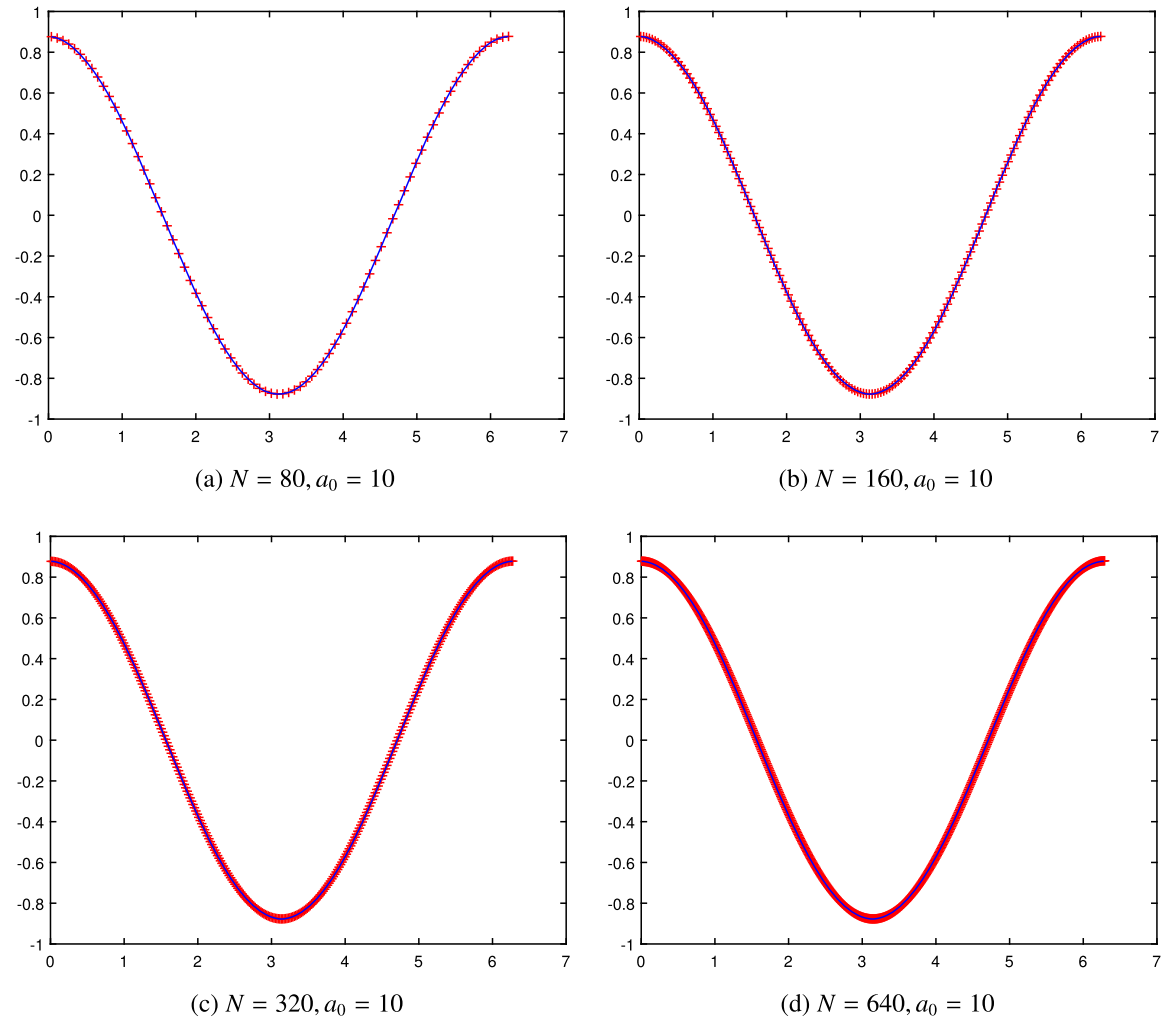

(a) $N = 80, a_0 = 10$ (b) $N = 160, a_0 = 10$

(c) $N = 320, a_0 = 10$ (d) $N = 640, a_0 = 10$

Fig. 2. The numerical solution of Eq. (20) with the exact solution Eq. (21) and periodic boundary condition at $t = 0.5$ using P^1 elements on the uniform mesh with 80, 160, 320 and 640 cells.

Table 3
The L^∞ errors and orders of accuracy for Example 3: $b(u) = 1 - \sin(x)$.

	N	$a_0 = 0.5$		$a_0 = 1$		$a_0 = 2$		$a_0 = 10$	
		L^∞ error	Order	L^∞ error	Order	L^∞ error	Order	L^∞ error	Order
P^0 with Eqs. (16)	10	9.94E-02	–	1.06E-01	–	1.18E-01	–	1.08E-01	–
	20	4.84E-02	1.04	5.28E-02	1.00	6.07E-02	0.96	5.32E-02	1.02
	40	2.40E-02	1.01	2.64E-02	1.00	3.08E-02	0.98	2.64E-02	1.01
	80	1.20E-02	1.01	1.32E-02	1.00	1.55E-02	0.99	1.32E-02	1.00
	160	5.97E-03	1.00	6.61E-03	1.00	7.80E-03	0.99	6.58E-02	1.00
	320	2.98E-03	1.00	3.31E-03	1.00	3.91E-03	0.99	3.29E-03	1.00
	640	1.51E-03	1.00	1.66E-03	1.00	1.96E-03	1.00	1.65E-03	1.00
P^1 with Eqs. (17)	10	7.40E-03	–	7.45E-03	–	7.57E-03	–	8.16E-03	–
	20	2.30E-03	1.72	2.28E-03	1.71	2.34E-03	1.69	2.47E-03	1.72
	40	6.18E-04	1.90	6.13E-04	1.90	6.10E-04	1.94	6.49E-04	1.93
	80	2.18E-04	1.50	1.96E-04	1.51	1.96E-04	1.52	2.13E-04	1.61
	160	4.96E-05	2.14	4.96E-05	1.98	4.96E-05	1.98	4.96E-05	2.10
	320	1.33E-05	1.90	1.33E-05	1.90	1.33E-05	1.90	1.33E-05	1.90
	640	3.20E-06	2.06	3.20E-06	2.06	3.20E-06	2.06	3.20E-06	2.06

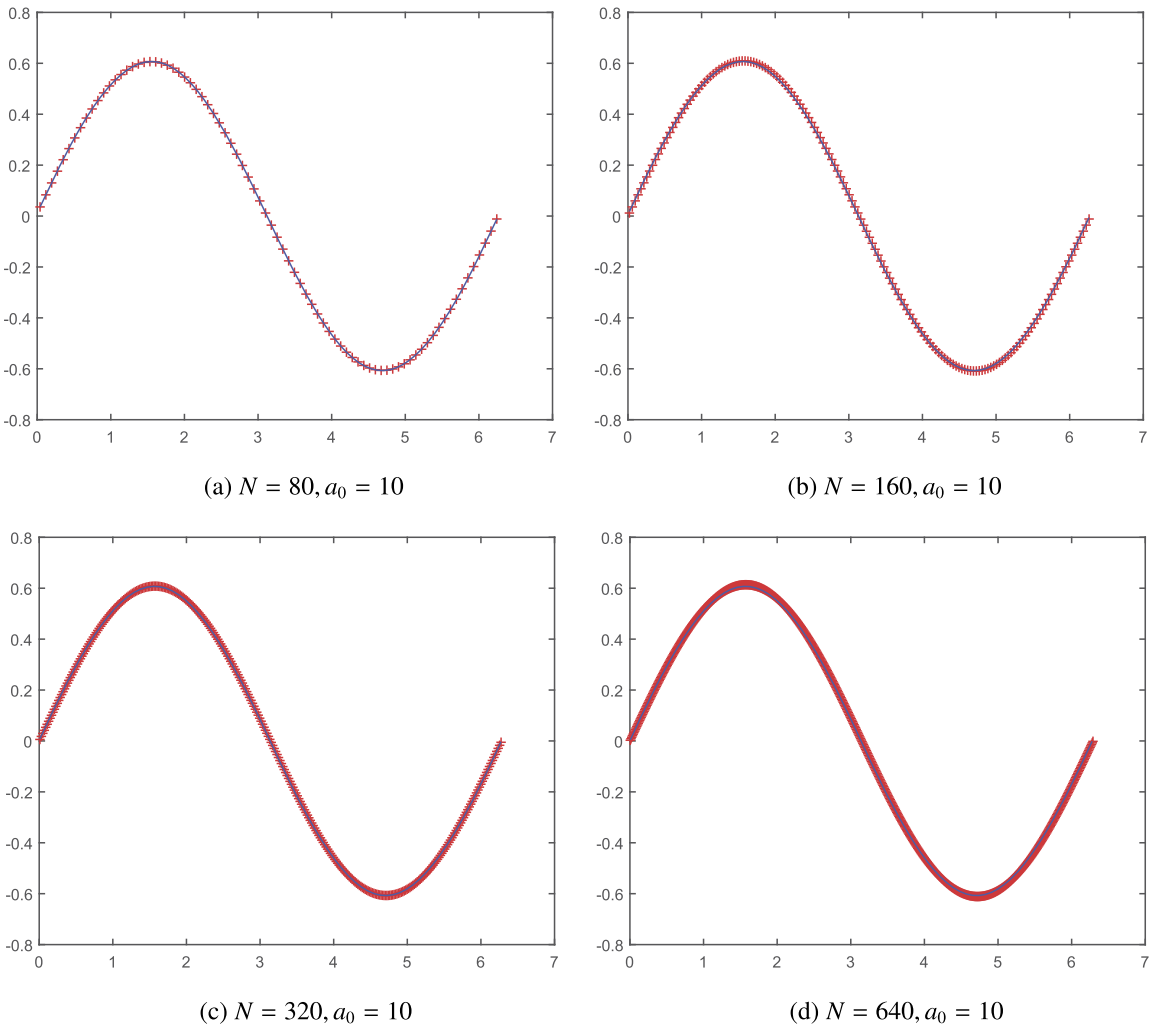

(a) $N = 80, a_0 = 10$ (b) $N = 160, a_0 = 10$

(c) $N = 320, a_0 = 10$ (d) $N = 640, a_0 = 10$

Fig. 3. The numerical solution of Eq. (22) with the exact solution Eq. (24) and periodic boundary condition at $t = 0.5$ using P^1 elements on the uniform mesh with 80, 160, 320 and 640 cells.

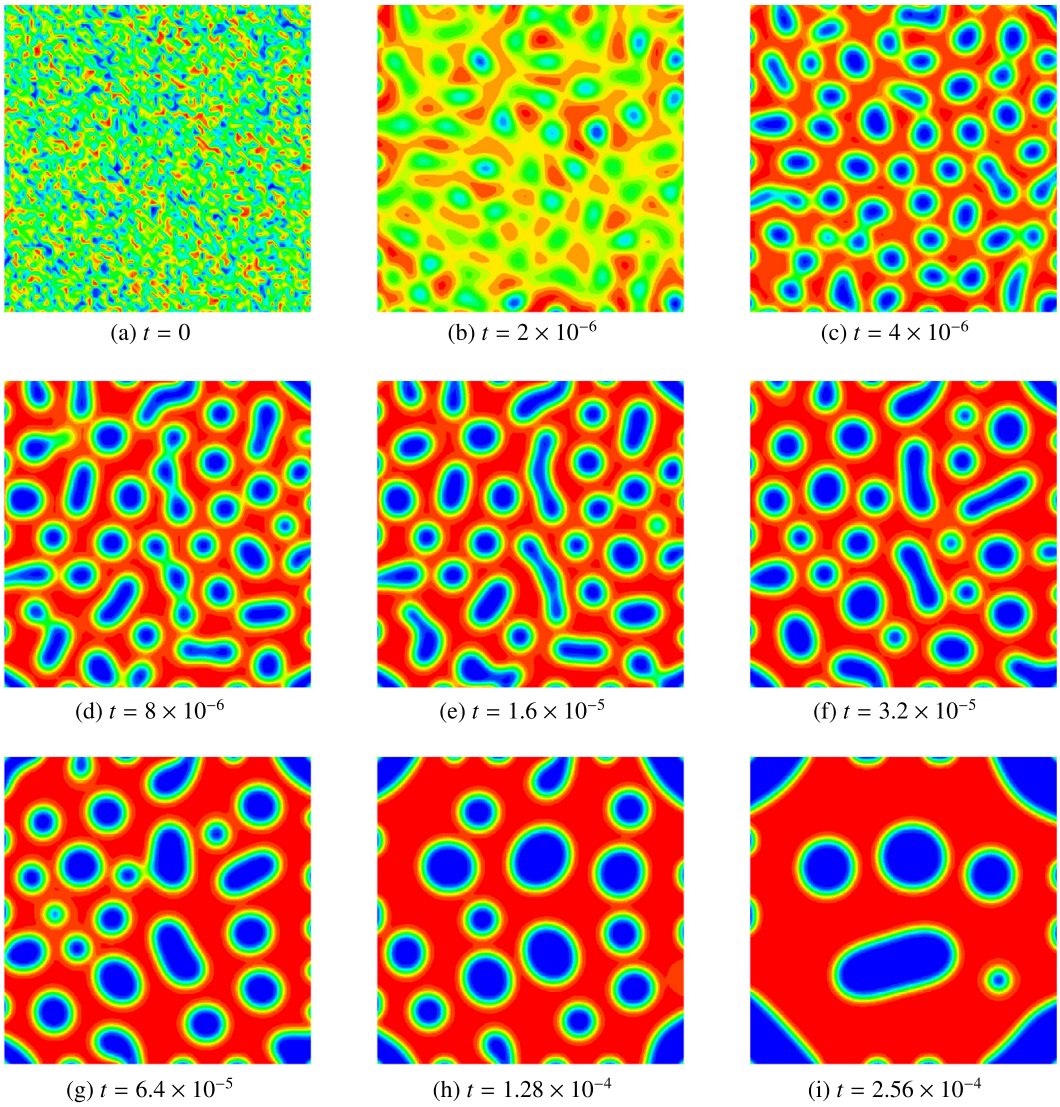

(a) $t = 0$ (b) $t = 2 \times 10^{-6}$ (c) $t = 4 \times 10^{-6}$

(d) $t = 8 \times 10^{-6}$ (e) $t = 1.6 \times 10^{-5}$ (f) $t = 3.2 \times 10^{-5}$

(g) $t = 6.4 \times 10^{-5}$ (h) $t = 1.28 \times 10^{-4}$ (i) $t = 2.56 \times 10^{-4}$

Fig. 4. The contours evolution of $u(x,t)$ for Eq. (25) at different time from a randomly perturbed initial condition with P^0 elements on the uniform mesh with 80×80 cells.

Example 4 *(Coarsening dynamics).* In the square domain $\Omega = (-0.5, 0.5) \times (-0.5, 0.5)$, we consider

$$u_t = \nabla \cdot \left(b(u) \nabla \left(-\gamma \Delta u + \Psi'(u) \right) \right) \tag{25}$$

with $b(u) = u(1-u)$, and $\gamma = 1$. The homogeneous free energy density is

$$\Psi(u) = 3000 \left(u \ln(u) + (1-u) \ln(1-u) \right) + 9000 u (1-u), \tag{26}$$

The boundary conditions are $\frac{\partial u}{\partial \boldsymbol{\nu}} = b(u) \nabla \omega \cdot \boldsymbol{\nu} = 0$ and the initial condition u_0 is a random perturbation of uniform state $u = 0.63$ with a fluctuation no larger than 0.05. We use the P^0 elements on a uniform mesh with 80×80 cells. The contours at different time are shown in Fig. 4. From Fig. 4, we observe that the concentration evolution can be categorized in two stages. The first stage is governed by phase separation, and the second stage is governed by phase coarsening (from $t = 8 \times 10^{-6}$ onwards). Meanwhile, the solution converges to a steady state after some time.

Example 5 *(Evolution of a square shape fluid).* We consider the Cahn-Hilliard equation

$$u_t = \nabla \cdot \left(b(u) \nabla \left(-\gamma \Delta u + \Psi'(u) \right) \right) \tag{27}$$

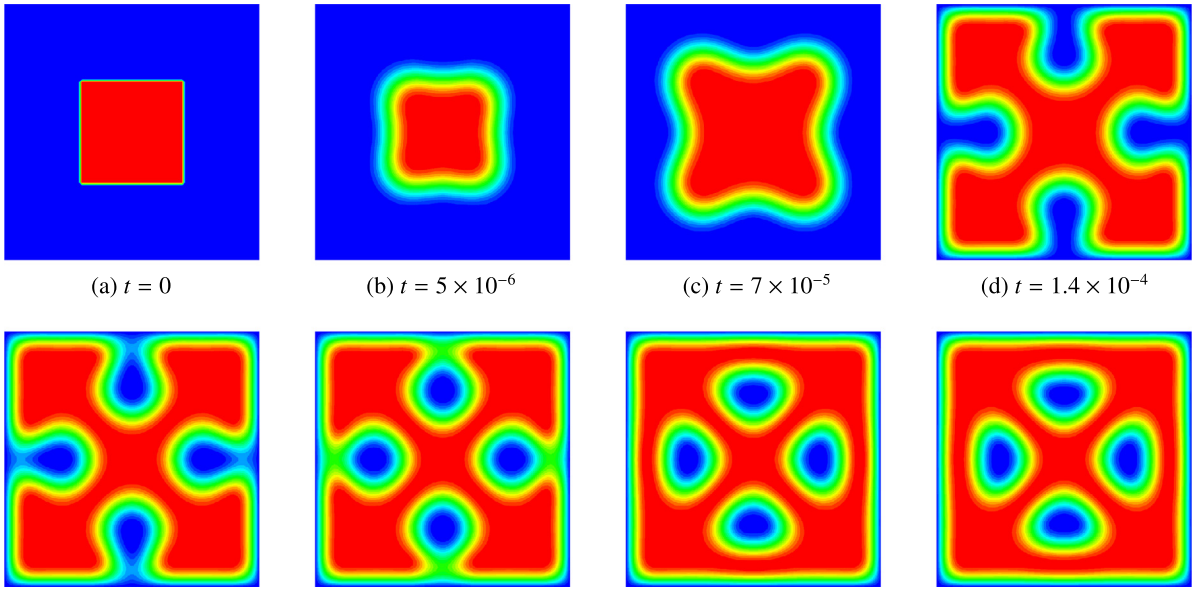

(a) $t = 0$ (b) $t = 5 \times 10^{-6}$ (c) $t = 7 \times 10^{-5}$ (d) $t = 1.4 \times 10^{-4}$

(e) $t = 1.5 \times 10^{-4}$ (f) $t = 1.6 \times 10^{-4}$ (g) $t = 1.7 \times 10^{-4}$ (h) $t = 1.8 \times 10^{-4}$

Fig. 5. The contours evolution of $u(x,t)$ for Eq. (27) at different time from the initial condition Eq. (29) with P^0 elements on the uniform mesh with 80×80 cells.

with $b(u) = 1$, and $\gamma = 1$. We take the homogeneous free energy density

$$\Psi(u) = 600\,(u \ln(u) + (1-u)\ln(1-u)) + 1800u\,(1-u)\,. \tag{28}$$

The initial condition is

$$u_0(\boldsymbol{x}) = \begin{cases} 0.71 & \boldsymbol{x} \in \Omega_1, \\ 0.69 & \boldsymbol{x} \in \Omega_2, \end{cases} \tag{29}$$

where the square domain

$$\Omega = (-0.5, 0.5) \times (-0.5, 0.5)\,, \Omega_1 = (-0.2, 0.2) \times (-0.2, 0.2)\,, \Omega_2 = \Omega - \Omega_1. \tag{30}$$

The boundary conditions are

$$\frac{\partial u}{\partial \boldsymbol{v}} = b(u)\nabla\omega \cdot \boldsymbol{v} = 0, \quad on \quad \partial\Omega. \tag{31}$$

We use the P^0 elements on the uniform mesh with 80×80 cells. The contours at different time are shown in Fig. 5. We can see that the square bubble in the fluid at $t = 0$ rapidly deforms into four circular bubbles. Compared with the numerical results presented in the literature [1], there is a satisfactory agreement of the global characteristics of the flow.

Example 6 *(Shape relaxation).* We consider the Cahn-Hilliard equation

$$u_t = \nabla \cdot \left(b\,(u)\,\nabla\left(-\gamma\,\Delta u + \Psi'\,(u)\right)\right) \tag{32}$$

where $b(u) = 1$, and $\gamma = 2 \times 10^{-5}$. The homogeneous free energy density is

$$\Psi(u) = \frac{1}{80}\left(u^2 - 1\right)^2. \tag{33}$$

We take the following initial condition

$$u_0(\boldsymbol{x}) = \begin{cases} 1 & \boldsymbol{x} \in \Omega_1, \\ -1 & \text{otherwise}, \end{cases} \tag{34}$$

where the square domain

$$\Omega = (-1, 1) \times (-1, 1)\,, \Omega_1 = (-0.5, 0.5) \times (-0.5, 0.5)\,, \Omega_2 = \Omega - \Omega_1. \tag{35}$$

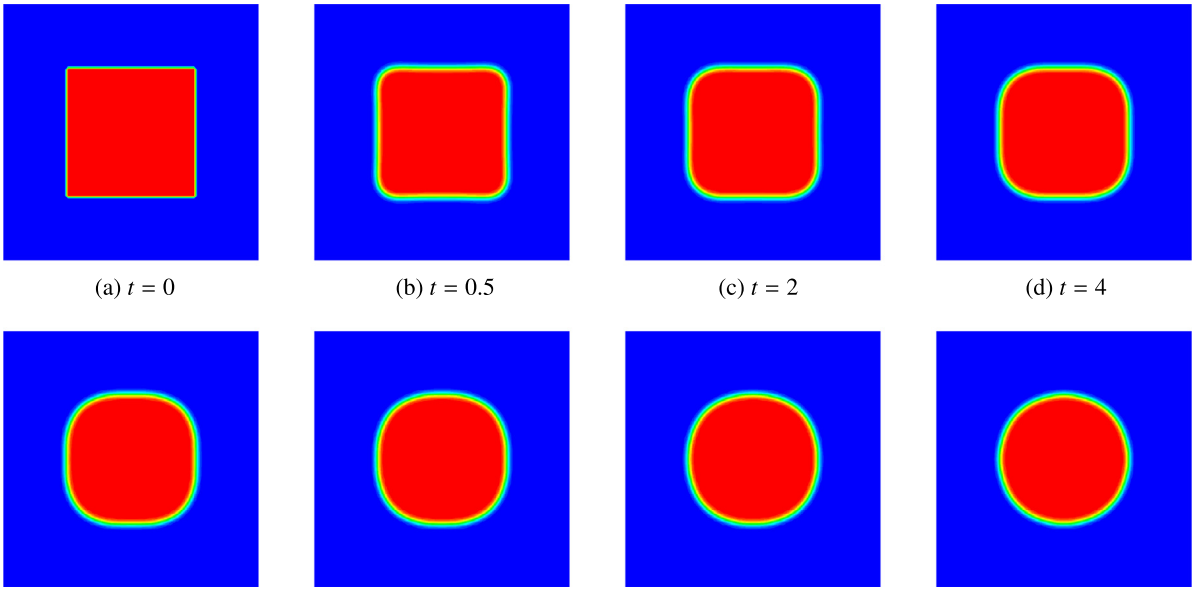

Fig. 6. The contours evolution of $u(x, t)$ for Eq. (32) at different time from the initial condition Eq. (34) with P^0 elements on the uniform mesh with 80×80 cells.

The boundary conditions are

$$\frac{\partial u}{\partial \boldsymbol{\nu}} = b(u)\nabla\omega \cdot \boldsymbol{\nu} = 0, \quad on \quad \partial\Omega. \tag{36}$$

We use the P^0 elements on the uniform mesh with 80×80 cells. The contours at different time are shown in Fig. 6. It is clear that the initial quare eventually evolves into a circle. Fig. 6 shows the similar numerical solution performed by Chen and Shen [12].

Example 7 *(Coalescence of two intersecting ellipses).* In the square domain $\Omega = (-0.4, 0.4) \times (-0.4, 0.4)$, we consider the Cahn-Hilliard equation

$$u_t = \nabla \cdot \left(b\left(u\right) \nabla \left(-\gamma \Delta u + \Psi'\left(u\right)\right)\right) \tag{37}$$

with $b(u) = 1$, and $\gamma = 0.1$. We take the homogeneous free energy density as follows

$$\Psi\left(u\right) = 250\left(u^2 - 1\right)^2. \tag{38}$$

The initial condition is

$$u_0\left(\boldsymbol{x}\right) = \tanh\left(\frac{1}{10^{-2}}\left(\frac{x_1^2}{0.0064} + \frac{x_2^2}{0.0225} - 1\right)\left(\frac{x_1^2}{0.0225} + \frac{x_2^2}{0.0064} - 1\right)\right) \tag{39}$$

The boundary conditions are

$$\frac{\partial u}{\partial \boldsymbol{\nu}} = \frac{\partial \Delta u}{\partial \boldsymbol{\nu}} = 0, \quad on \quad \partial\Omega. \tag{40}$$

Note that the initial set of u_0 is the union of the following two intersecting ellipses: $\frac{x_1^2}{0.0064} + \frac{x_2^2}{0.0225} = 1$ and $\frac{x_1^2}{0.0225} + \frac{x_2^2}{0.0064} = 1$, which enclose four bullethead-like bubbles inside a fluid.

We use the P^0 elements on the uniform mesh with 80×80 cells. The contours at different time are shown in Fig. 7. From Fig. 7, we observe that the initial fluid bubble first splits into four bubbles, then they deform into four circles, and finally merge to form two circular bubbles. Compared with the respective patterns displayed by Feng [13], there is a similar evolution of the bubbles.

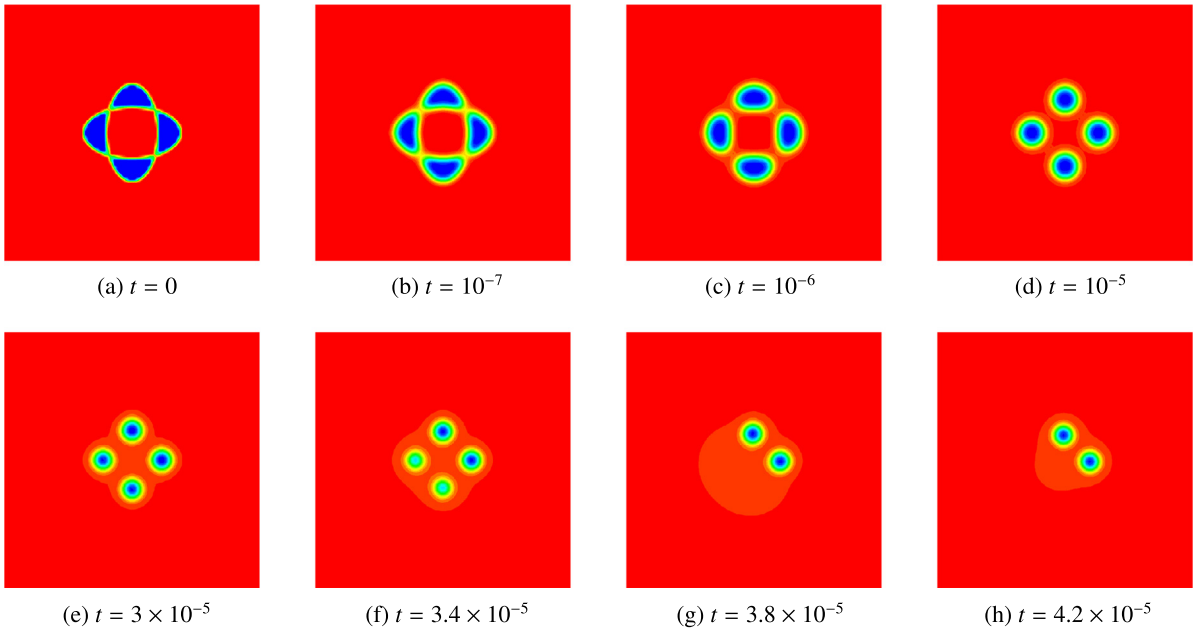

Fig. 7. The contours evolution of $u(x,t)$ for Eq. (37) at different time from the initial condition Eq. (39) with P^0 elements on the uniform mesh with 80×80 cells.

4. Conclusion

In this paper, we have proposed a class of IMEX multistep LDG schemes for solving the nonlinear Cahn-Hilliard equation. A new form of the equation is constructed by adding and subtracting a "linear" term $a_0\Delta\beta$ on the right hand side of the second order system. Given the nonlinear function $\Psi'(u)$ in $a_0\Delta\beta$, we make some extra treatments during the discretizaiton. The LDG method, using linear and quadratic basis functions, is adopted for spatial discretization. And the IMEX multistep method is used for temporal discretization. To verify the correctness of the methods, we applied schemes to the test experiments previously considered in the literatures. Compared with the numerical results of some established methods, ours show that the schemes are stable and efficient. Meanwhile, there is no obvious difference for different value of a_0 in the numerical experiments.

Acknowledgements

The authors would like to thank Dr. Ying Li (Shanghai University) for her insightful comments and suggestions. This research was supported by NSF of China (No. 11601315) and Shanghai Sailing Program (No. 16YF1404000).

References

[1] Y. Xia, Y. Xu, C.-W. Shu, Local discontinuous Galerkin methods for the Cahn-Hilliard type equations, J. Comput. Phys. 227 (1) (2007) 472–491.
[2] J.W. Cahn, J.E. Hilliard, Free energy of non-uniform system. I. Interfacial free energy, J. Chem. Phys. 28 (1958) 258–267.
[3] X. Yang, J. Zhao, Efficient linear schemes for the nonlocal Cahn-Hilliard equation of phase field models, Comput. Phys. Commun. 235 (2019) 234–245.
[4] J. Shen, J. Xu, J. Yang, The scalar auxiliary variable (SAV) approach for gradient flows, J. Comput. Phys. 353 (2018) 407–416.
[5] Y. Chen, J. Lowengrub, J. Shen, C. Wang, S. Wise, Efficient energy stable schemes for isotropic and strongly anisotropic Cahn-Hilliard systems with the Willmore regularization, J. Comput. Phys. 365 (2018) 56–73.
[6] X. Yang, J. Zhao, X. He, Linear, second order and unconditionally energy stable schemes for the viscous Cahn-Hilliard equation with hyperbolic relaxation using the invariant energy quadratization method, J. Comput. Appl. Math. 343 (2018) 80–97.
[7] Q. Du, L. Ju, X. Li, Z. Qiao, Stabilized linear semi-implicit schemes for the nonlocal Cahn-Hilliard equation, J. Comput. Phys. 363 (2018) 39–54.
[8] J. Shin, H. Lee, J.-Y. Lee, Unconditionally stable methods for gradient flow using convex splitting Runge-Kutta scheme, J. Comput. Phys. 347 (2017) 367–381.
[9] D. Li, Z. Qiao, On second order semi-implicit Fourier spectral methods for 2D Cahn-Hilliard equations, J. Sci. Comput. 70 (2017) 301–341.
[10] H. Song, C.-W. Shu, Unconditional energy stability analysis of a second order implicit-explicit local discontinuous Galerkin method for the Cahn-Hilliard equation, J. Sci. Comput. 73 (2–3) (2017) 1178–1203.
[11] R. Guo, Y. Xia, Y. Xu, Semi-implicit spectral deferred correction methods for highly nonlinear partial differential equations, J. Comput. Phys. 338 (2017) 269–284.
[12] Y. Chen, J. Shen, Efficient, adaptive energy stable schemes for incompressible Cahn-Hilliard Navier-Stokes phase-field models, J. Comput. Phys. 380 (2016) 40–56.
[13] X. Feng, Fully discrete finite element approximations of the Navier-Stokes-Cahn-Hilliard diffuse interface model for two-phase fluid flows, SIAM J. Numer. Anal. 44 (3) (2006) 1049–1072.
[14] Y. Xia, Y. Xu, C.-W. Shu, Local discontinuous Galerkin methods for the generalized Zakharov system, J. Comput. Phys. 229 (2010) 1238–1259.

[15] Y. Xu, C.-W. Shu, Local discontinuous Galerkin methods for the Kuramoto-Sivashinsky equations and the Ito-type coupled KdV equations, Comput. Methods Appl. Mech. Eng. 195 (2006) 3430–3447.
[16] J. Yan, C.-W. Shu, A local discontinuous Galerkin method for KdV type equations, SIAM J. Numer. Anal. 40 (2002) 769–791.
[17] B. Cockburn, C.-W. Shu, The local discontinuous Galerkin method for time-dependent convection-diffusion systems, SIAM J. Numer. Anal. 35 (6) (1998) 2440–2463.
[18] F. Bassi, S. Rebay, A high-order accurate discontinuous finite element method for the numerical solution of the compressible Navier-Stokes equations, J. Comput. Phys. 131 (2) (1997) 267–279.
[19] J. Yan, C.-W. Shu, Local discontinuous Galerkin methods for partial differential equations with high order derivatives, J. Sci. Comput. 17 (1–4) (2002) 27–47.
[20] B. Cockburn, C.-W. Shu, Runge-Kutta discontinuous Galerkin methods for convection-dominated problems, J. Sci. Comput. 16 (3) (2001) 173–261.
[21] B. Cockburn, C.-W. Shu, TVB Runge-Kutta local projection discontinuous Galerkin finite element method for conservation laws. II: general framework, Math. Comput. 52 (186) (1989) 411–435.
[22] B. Cockburn, S.-Y. Lin, C.-W. Shu, TVB Runge-Kutta local projection discontinuous Galerkin finite element method for conservation laws. III: one-dimensional systems, J. Comput. Phys. 84 (1989) 90–113.
[23] B. Cockburn, S.C. Hou, C.-W. Shu, The Runge-Kutta local projection discontinuous Galerkin finite element method for conservation laws. IV: the multi-dimensional case, Math. Comput. 54 (190) (1990) 545–581.
[24] B. Cockburn, C.-W. Shu, The Runge-Kutta discontinuous Galerkin method for conservation laws. V: multidimensional systems, J. Comput. Phys. 141 (1998) 199–224.
[25] B. Seibold, D. Shirokoff, D. Zhou, Unconditional stability for multistep ImEx schemes-practice, J. Comput. Phys. 376 (2019) 295–321.
[26] H. Wang, Q. Zhang, S. Wang, C.-W. Shu, Local discontinuous Galerkin methods with explicit-implicit-null time discretizations for solving nonlinear diffusion problems, Sci. China Math. 63 (2020), https://doi.org/10.1007/s11425-018-9524-x.
[27] H. Wang, Q. Zhang, C.-W. Shu, Third order implicit-explicit Runge-Kutta local discontinuous Galerkin methods with suitable boundary treatment for convection-diffusion problems with Dirichlet boundary conditions, J. Comput. Appl. Math. 342 (2018) 164–179.
[28] R.R. Rosales, B. Seibold, D. Shirokoff, D. Zhou, Unconditional stability for multistep imex schemes-theory, SIAM J. Numer. Anal. 55 (5) (2017) 2336–2360.
[29] H. Wang, Q. Zhang, C.-W. Shu, Stability analysis and error estimates of local discontinuous Galerkin methods with implicit-explicit time-marching for the time-dependent fourth order PDEs, ESAIM Math. Model. Numer. Anal. 51 (2017) 1931–1955.
[30] H. Wang, C.-W. Shu, Q. Zhang, Stability analysis and error estimates of local discontinuous Galerkin methods with implicit-explicit time-marching for nonlinear convection-diffusion problems, Appl. Math. Comput. 272 (2016) 237–258.
[31] H. Wang, S. Wang, Q. Zhang, C.-W. Shu, Local discontinuous Galerkin methods with implicit-explicit time-marching for multi-dimensional convection-diffusion problems, ESAIM Math. Model. Numer. Anal. 50 (2016) 1083–1105.
[32] Y. Gao, L. Mei, Implicit-explicit multistep methods for general two-dimenisonal nonlinear Schrödinger equations, Appl. Numer. Math. 109 (2016) 41–60.
[33] H. Wang, C.-W. Shu, Q. Zhang, Stability and error estimates of local discontinuous Galerkin methods with implicit-explicit time-marching for advection-diffusion problems, SIAM J. Numer. Anal. 53 (2015) 206–227.
[34] H. Song, Energy SSP-IMEX Runge-Kutta methods for the Cahn-Hilliard equation, J. Comput. Appl. Math. 292 (2016) 576–590.
[35] Y. He, Y. Liu, T. Tang, On large time-stepping methods for the Cahn-Hilliard equation, Appl. Numer. Math. 57 (2007) 616–628.
[36] Y. He, W. Sun, Stability and convergence of the Crank-Nicolson/Adams-Bashforth scheme for the time-dependent Navier-Stokes equations, SIAM J. Numer. Anal. 45 (2007) 837–869.
[37] Y. He, The Euler implicit/explicit scheme for the 2D time-dependent Navier-Stokes equations with smooth or non-smooth initial data, Math. Comput. 77 (2008) 2097–2124.
[38] C. Xia, Y. Li, H. Wang, Local discontinuous Galerkin methods with explicit Runge-Kutta time marching for nonlinear carburizing model, Math. Methods Appl. Sci. (2008).